Optics Letters

Proposal of phase noise and jitter reduction in a long-ring hybrid silicon mode-locked laser by intracavity reflectors

MOHAMMAD SHEKARPOUR AND MOHAMMAD HASAN YAVARI*

Faculty of Engineering, Shahed University, Tehran, Iran
**Corresponding author: mh.yavari@shahed.ac.ir*

Received 24 February 2021; revised 8 May 2021; accepted 8 May 2021; posted 13 May 2021 (Doc. ID 422853); published 14 June 2021

We propose a harmonically hybrid silicon mode-locked ring laser using intracavity reflectors (ICRs) to suppress supermode noise. The dynamic and noise properties of the structure are investigated using a delay differential equation model. The results of the dynamic show that a 20 GHz harmonic regime of the structure is significantly increased compared to a without intracavity–reflector structure. Additionally, the phase noise of the proposed structure (PS) is improved to about 8 dB. Furthermore, an analysis shows that timing jitter reduction has periodic behavior by changing the harmonic inter-spike interval time (T_{ISI}).

https://doi.org/10.1364/OL.422853

The generation of an optical pulse train at high-frequency has been attracting much interest in the past several decades [1–7]. Low phase noise operation of mode-locked lasers (MLLs) for applications such as analog-to-digital converters [8] and optical clocking [9] is a topic of interest. Low-noise operation of a MLL can be achieved with long cavity structures due to their high quality factor [10]. Integrated photonic passive waveguides make long on-chip cavities possible, as well as reducing the cavity loss which is crucial in designing a long-ring MLL (LR-MLL) [11,12]. In these lasers, to obtain a desired high-frequency repetition rate, harmonic mode-locked operation is required in many applications [8]. By applying the proper pumping current and absorber voltage in a LR-MLL, harmonic mode locking (HML) can be obtained. However, the intermediate longitudinal modes are not suppressed sufficiently, which leads to amplitude distortions in the pulse train [11,13]. Additionally, the number of harmonics can be changed by changing the voltage and pumping current. In [11], by implementing an intracavity filter at a LR-MLL, as an effective method to suppress the noise caused by independent propagation of multiple pulses circulating at the cavity roundtrip frequency, the RF linewidth is reduced to 52 KHz. In this method, the stability regime of the tenth harmonic (H_{10}) is significantly increased, compared to a without intracavity filter structure [14].

In this Letter, we propose a modification of a LR-MLL by using intracavity reflectors (ICRs) to produce HML. The influence of ICRs on the dynamic behavior of a passively mode-locked hybrid silicon laser is investigated. The timing jitter and phase noise of the proposed structure (PS) are simulated and compared with a without intracavity–reflector structure (WOICRS).

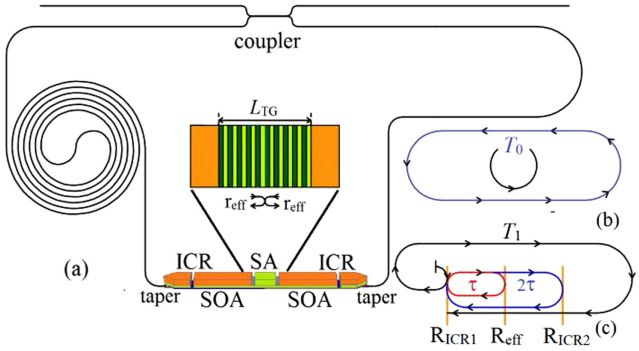

Fig. 1. (a) Schematic of the PS and corresponding paths for time delays used for the DDE model in the (b) WOICRS and (c) PS.

As shown in Fig. 1(a), the PS has two gain sections separated by a saturable absorber (SA). A 10:90 directional coupler couples light from a ring laser to a bus waveguide. The propagation loss of the waveguide is about 1 dB/cm. The low-propagation loss silicon waveguide is an effective method for achieving a high quality factor and therefore better sidemode suppression. The PS consists of a combination of linear and ring configurations due to the existence of ICRs. Because of two intermediate reflectors positioned on both sides of SA symmetrically, this design is symmetrical; consequently, the pulse train can be generated in clockwise and counter-clockwise direction. Note that the symmetric ICRs can be considered as a Fabry–Perot (FP) cavity.

To achieve low-noise operation in HML, the structure must be designed passively so that the maximum suppression of intermediate modes occurred. The multiple circulations of optical field inside the ring resonator are physically identical to the multiple reflections inside a linear cavity [15]. Therefore, to investigate the influence of the FP cavity on the filtering behavior of the PS, we use the equivalent optical circuit. The ring resonator with and without the FP cavity, as well as the equivalent linear cavity, is shown in Fig. 2. The roundtrip time of the FP cavity is designed to be half of the desired repetition rate (20 GHz). The length ratio of the FP cavity and the ring cavity is $L_{FP}:L_{ring} = m:n$. If m and n are considered as an integer

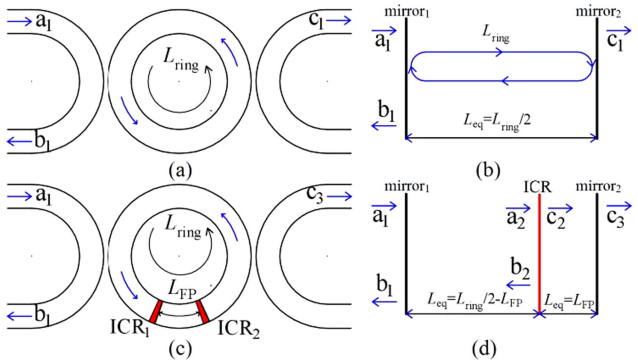

Fig. 2. Ring resonator and equivalent linear cavity for (a), (b) without and (c), (d) with the FP cavity.

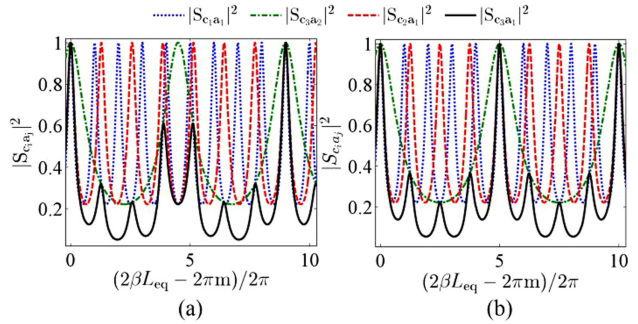

Fig. 3. Magnitude of the transmission coefficient ($\mathrm{Sc}_i a_j$) for the length ratio (L_{FP}:L_{ring}) of (a) 2/9 and (b) 2/10.

value without a common factor, the intermediate mode of the ring cavity can be better suppressed by a FP cavity filter [16]. Thus, the length ratio can be selected as 2/9 or 2/11. Figures 3(a) and 3(b) show. the magnitude of the transmission coefficient ($|\mathrm{Sc}_i a_j|^2 = |c_i/a_j|^2$) versus $2\beta L_{\mathrm{eq}}$ (where β is propagation constant) for $L_{\mathrm{FP}}/L_{\mathrm{ring}} = 2/9$ and 2/10, respectively. As can be seen, for $L_{\mathrm{FP}}/L_{\mathrm{ring}} = 2/10$, the fifth mode of the ring is not suppressed due to a common factor of 2 and 10. In the ML regime, $L_{\mathrm{FP}}/L_{\mathrm{ring}} = 2/9$ in the PS leads to generation of the pulse train with 20 GHz, which is H_9 of fundamental frequency. Additionally, the FP cavity constructed by ICRs operates such as two sub-cavities with a length ratio of 1/9, due to symmetric colliding pulse effects in the SA. Thus, the suppression of mode in the PS is higher compared to the structure introduced in [11] which has one intracavity filter with a length ratio of 1/10.

Based on the model proposed in [17], in this Letter, we extend the delay differential equation (DDE) model to study HML of the PS and WOICRS [Figs. 1(b) and 1(c)]. Equations (1) and (2) describe the slowly varying field amplitude E in the WOICRS and PS, respectively. The final set of three coupled DDEs for the field amplitude E, the saturable gain G, and the saturable loss Q are

$$\gamma^{-1}\dot{E}(t) = -E(t) + R_0(t - T_0)e^{-i\Delta\Omega T_0}E(t - T_0) + D\xi(t), \quad \textbf{(1)}$$

$$\gamma^{-1}\dot{E}(t) = -E(t) + R_1(t - T_1)e^{-i\Delta\Omega T_1}E(t - T_1) + \sum_{l=1}^{\infty} e^{-ilc - i\Delta\Omega(T_1 + l\tau)}R_2(t - T_1 - l\tau) \times E(t - T_1 - l\tau) + \sum_{l=1}^{\infty} e^{-i2lc - i\Delta\Omega(T_1 + 2l\tau)} \times R_3(t - T_1 - l(2\tau))E(t - T_1 - l(2\tau)) + D\xi(t), \quad \textbf{(2)}$$

$$\dot{G}(t) = J_g - \gamma_g G(t) - e^{-Q(t)}(e^{G(t)} - 1)|E(t)|^2, \quad \textbf{(3)}$$

$$\dot{Q}(t) = J_q - \gamma_q Q(t) - r_s e^{-Q(t)}(e^{G(t)} - 1)|E(t)|^2, \quad \textbf{(4)}$$

$$R_i(t) = \sqrt{k_i}e^{1/2(1 - i\alpha_g)G(t) - 1/2(1 - i\alpha_q)Q(t)} \quad i = 0, 1, 2, 3, \quad \textbf{(5)}$$

where Eqs. (1), (3), and (4) model the WOICRS [Fig. 1(b)], and Eqs. (2)–(4) model the PS [Fig. 1(c)].

As shown in Fig. 1(a), the clockwise and counter-clockwise pulses collide within the SA and, consequently, transient grating (TG) is produced [18]. For modeling TG of colliding-pulse mode-locking (CPM), we define the effective mirror model. The effective length (L_{eff}) of TG is $L_{\mathrm{eff}} = \tanh(\kappa L_{\mathrm{TG}})$ [19], where κ is the coupling coefficient. For the small index difference of TG ($\tanh \kappa L_{\mathrm{TG}} \to \kappa L_{\mathrm{TG}}$), the effective mirror is at the center of the TG. Additionally, the absorption of TG is modeled by Q in DDEs. It should be noted that there is no reflectors in the WOICRS, so the part of the optical field reflected by TG cannot be taken into account in a unidirectional DDE model. However for the PS, definition of the effective mirror is vital due to the existence of ICRs. Thus, the delay time of the WOICRS is T_0 and for the PS, the DDE is based on three delay time $T_1 = 0.9\,T_0$, $\tau = 0.1\,T_0$ and 2τ.

Here l is the number of roundtrips between the ICR and effective mirror, and C is the phase of the light due to one roundtrip. $\Delta\Omega$ accounts for a possible detuning between the frequency of the maximum of the gain spectrum and the frequency of the nearest cavity mode. The linewidth enhancement factors in the gain and absorber sections are denoted by α_g and α_q, respectively. Spontaneous emission is modeled in (1) and (2) by a complex Gaussian white-noise term $\xi(t)$ with strength D. In (5), $R_i(t)$ describes the amplification and losses of the electric field during one roundtrip in the WOICRS and PS. The cavity intensity loss for the WOICRS is $kk_0 = C_f + (LL_w) + Lc + S_c$; for the PS, the cavity intensity losses ($l = 1$) are $kk_1 = C_f + (0.9LL_w) + Lc + S_c + R_{\mathrm{ICR}}$, $kk_2 = C_f + (LL_w) + Lc + S_c + R_{\mathrm{eff}}$ and $kk_3 = C_f + (1.1LL_w) + Lc + S_c + R_{\mathrm{ICR}}$. The relation between kk_i and k_i is $kk_i = 10\log k_i$. The other parameters for the simulations are given in Table 1.

The timing fluctuations of pulses are appeared in $T_{\mathrm{ISI,Hn}}$, so the calculations of the phase noise and timing jitter are based on this factor. The $T_{\mathrm{ISI,H1}} \approx T_0 + O(\gamma^{-1})$ of fundamental frequency is longer than the cold-cavity roundtrip time T_0 [17]. For H_{10} frequency, $T_{\mathrm{ISI,H10}} \approx (T_0 + O(\gamma^{-1}))/10$. Figure 4 depicts the simulated output of the WOICRS in the H_{10} ML regime. The optical period of pulses is divided into a slow stage

Table 1. Parameters Used in Numerical Simulations [3,5,11]

Symbol	Quantity	Value
γ	Full width at half-maximum	0.125 ps^{-1}
γ_g	Carrier relaxation rate in gain section	1 ns^{-1}
γ_q	Carrier relaxation rate in absorber section	75 ns^{-1}
r_s	Ratio of saturation energies	25
J_g	Pump rate in gain section	1–160
J_q	Pump rate in absorber section	50–400
L	Cavity length of ring laser	3.967 cm
L_w	Propagation loss of waveguide	1 dB/cm
L_c	Propagation loss of coupler	0.5 dB
S_c	Splitting ratio of coupler	10 dB
T_0, T_1	Cavity roundtrip time	500, 450 ps
$T_{\mathrm{ISI,H1}}$	Inter-spike interval time	1.005 T_0
C_f	Correction factor	4.7 dB
τ	Intracavity roundtrip time	0.1 T_0
R_{ICR}	Intensity reflection of intracavity reflector	10 dB
D	Strength of spontaneous emission noise	0.1e4

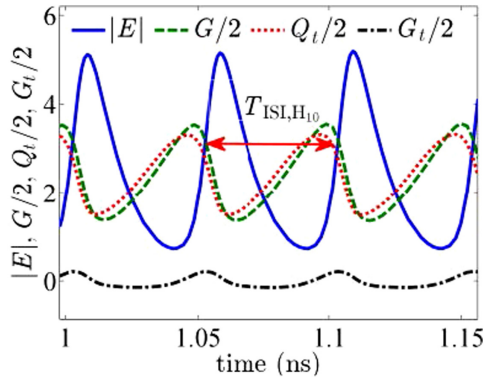

Fig. 4. Time traces of the amplitude $|E|$, gain G, total loss Q_t, and net gain G_t.

($|E|^2 \sim 0$), in which gain and absorption media are recovered, and a fast stage, in which the electric field intensity is large [17]. In the H_{10} regime, the slow stage is shorter, and the fast stage is longer than the fundamental mode-locking (FML) regime. Considering H_{10} of WOICRS, Fig. 4 shows time traces of the amplitude $|E|$, the total loss $Q_t \equiv Q + |\ln k_0|$, the saturable gain G, and the net gain $G_t \equiv G(t) - Q_t$. Due to the lower recovery time of absorbing media compared with gain media, the absorbing section saturated faster; therefore, net gain is positive, which is necessary to compensate for cavity roundtrip losses [17].

To investigate resonance regions where the greater phase noise reduction is occurred, determination of the 20 GHz harmonic regime is essential. In this regard, the dynamic regimes of FML, HML, continuous-wave (CW), and Q-switching (QS) for the PS and WOICRS are illustrated in Fig. 5. In the WOICRS with ~2 GHz fundamental frequency, a gradual transition from H_1 to H_{10} is observed with an increase of J_g and J_q. According to the experimental results [1,13], by increasing the voltage of the absorber, the ML operation changes from higher to lower harmonic frequency; therefore, the pumping current must be increased to achieve desired harmonic. Figure 5(a) clearly shows this behavior. However in the PS with ~2.22 GHz fundamental

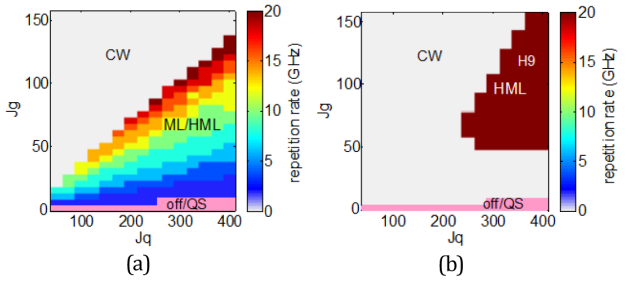

Fig. 5. Repetition frequency; (a) WOICRS, (b) PS.

frequency, the HML regime exhibits only H_9 owing to FP filter selectivity. The H_9 regime of the PS is generated in lower J_g and J_q, and is significantly increased compared to the WOICRS. Furthermore, considering a with-intracavity structure [11,14], a 20 GHz harmonic regime of the PS is increased.

By considering spontaneous emission noise ($D \neq 0$), the fluctuations in arrival times of pulses are appeared. By using the procedure proposed in [20], these fluctuations can be quantified by the root-mean-square (rms)-timing jitter. For each realization j of noise, the timing fluctuation $\{\Delta t\}_j$ is defined by timing deviations $t_p - p\langle T_{\mathrm{ISI,Hn}}\rangle$ of the pulse train from an ideal clock with a repetition period $\langle T_{\mathrm{ISI,Hn}}\rangle$, where t_p is the arrival time of the pth pulse. The repetition period of an ideal clock $\langle T_{\mathrm{ISI,Hn}}\rangle$ is obtained by first averaging the $T_{\mathrm{ISI,Hn}}$ over the number N of the pulse train and subsequently averaging over M noise realization of the timing jitter. In simulations, pulse trains containing $N = 3 \times 10^4$ pulses are used. The discrete Fourier transform is applied to each realization of the timing fluctuations $\{\Delta t\}_j$. Consequently, by averaging over M noise realization, the timing spectral density is obtained [20]:

$$\langle |\hat{\Delta}t(v)|^2 \rangle \equiv \frac{1}{M}\sum_{j=1}^{M} \Delta T \left| \frac{1}{N}\sum_{p=1}^{N} \{\Delta t\}_j e^{-i2\pi v l \langle T_{\mathrm{ISI,Hn}}\rangle} \right|^2, \quad (6)$$

where the time span $\Delta T \equiv N\langle T_{\mathrm{ISI,Hn}}\rangle$. The phase noise spectrum is related to the timing spectral density:

$$L(v) \equiv \left(\frac{2\pi}{\langle T_{\mathrm{ISI,Hn}}\rangle}\right)^2 \langle |\hat{\Delta}t(v)|^2 \rangle, \quad (7)$$

by integrating the phase noise spectrum $L(v)$ over the frequency range from v_{low} to v_{high}, the rms-timing jitter is defined as

$$\sigma_{\mathrm{rms}}(v_{\mathrm{low}}, v_{\mathrm{high}}) \equiv \frac{\langle T_{\mathrm{ISI,Hn}}\rangle}{2\pi} \sqrt{\int_{v_{\mathrm{low}}}^{v_{\mathrm{high}}} 2L(v)\mathrm{d}v}, \quad (8)$$

where v_{low} and v_{high} are the minimum and maximum frequency offsets from the repetition frequency of the ideal clock $1/\langle T_{\mathrm{ISI,Hn}}\rangle$. Since the spectrum is assumed to be symmetric, by a factor of 2 in (8), the full timing jitter can be calculated from integrating only over the phase noise of a single sideband. The phase noise spectrum is obtained for a WOICRS and the PS by averaging over $M = 30$ noise realizations. Subsequently, the rms-timing jitter is calculated by integrating the phase noise spectrum over the frequency range from $v_{\mathrm{low}} = 0.5$ MHz to $v_{\mathrm{high}} = 5$ GHz.

The single sideband phase noise of both the WOICRS and the PS are plotted in Fig. 6. It can be seen that the phase noise is

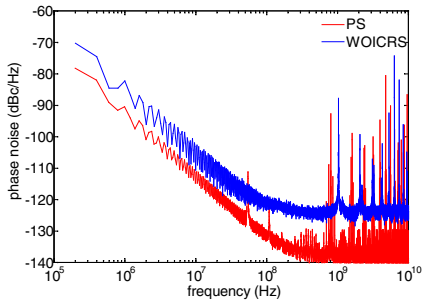

Fig. 6. Single sideband phase noise of the WOICRS and the PS for $J_g = 130$ and $J_q = 400$.

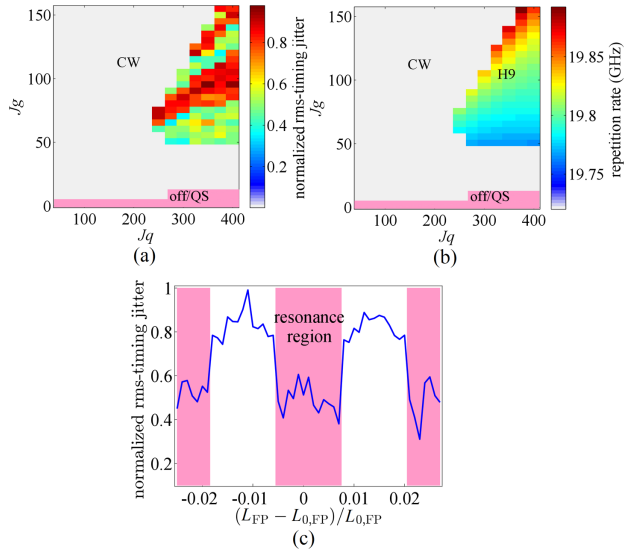

Fig. 7. (a) Rms-timing jitter of the PS that is normalized to the rms-timing jitter of the WOICRS, (b) repetition frequency of the PS in the H_9 regime and (c) normalized rms-timing jitter as a function of distance between ICRs for constant $J_g = 60$ and $J_q = 400$.

improved about 8 dB. The rms-timing jitter of the PS normalized to the rms-timing jitter of the WOICRS as a function of J_g and J_q, is shown in Fig. 7(a). As can be seen, the rms-timing jitter of the PS is decreased compared to the WOICRS. Indeed, the use of a FP filter in the PS leads to suppression of the supermode noise and therefore a reduction of the phase noise and rms-timing jitter. Furthermore, considering the dynamic results (Fig. 5), a 20 GHz frequency repetition rate of the PS can be achieved at a much lower pumping current due to two subcavity filters. Thus, the spontaneous emission noise decreases, and further reduction of the phase noise and rms-timing jitter is achieved.

In this figure, the periodic behavior of the rms-timing jitter is obvious. Additionally in a 20 GHz harmonic regime (H_9) of the PS, by changing J_g and J_q, the repetition rate frequency, and consequently $T_{ISI,H9}$, is changed [Fig. 7(b)]. By considering this variation, we find that the rms-timing jitter is highly sensitive to the ratio between T_1 and $T_{ISI,H9}$. Thus, a greater rms-timing jitter reduction is obtained in the resonance region. To clarify the dependence of the rms-timing jitter on $T_{ISI,H9}$, the influence of distance between ICRs as an important factor in determining $T_{ISI,H9}$ is investigated. The normalized rms-timing jitter as a function of L_{FP} is shown in Fig. 7(c) for constants $J_g = 60$ and $J_q = 400$. As can be seen in Fig. 7(c), the normalized rms-timing jitter, like the pattern of Fig. 7(a), has periodic behavior. Therefore, changes in $T_{ISI,H9}$ lead to resonance and nonresonance regions that affect the stability of pulses as well as the rms-timing jitter.

In conclusion, a long-ring MLL on silicon substrate with symmetric ICRs is presented. The dynamic, phase noise, and rms-timing jitter of the WOICRS and the PS are investigated by a DDE model. A 20 GHz harmonic regime can be achieved for the WOICRS and the PS in H_{10} and H_9, respectively. Based on a dynamic analysis of repetition frequency, we show that the H_9 regime of the PS is significantly increased compared to the H_{10} regime of the WOICRS. Additionally, the phase noise and rms-timing jitter are reduced compared to the WOICRS. Furthermore, the numerical results of periodic behavior of the rms-timing jitter show that the greater reduction occurred in resonance region.

Disclosures. The authors declare no conflicts of interest.

Data Availability. Data underlying the results presented in this paper are not publicly available at this time but may be obtained from the authors upon reasonable request.

REFERENCES

1. S. Arahira, Y. Matsui, and Y. Ogawa, IEEE J. Quantum Electron. **32**, 1211 (1996).
2. E. A. Avrutin, J. H. Marsh, and E. L. Portnoi, IEE Proc. Optoelectron. **147**, 251 (2000).
3. U. Bandelow, M. Radziunas, A. Vladimirov, B. Huttl, and R. Kaiser, Opt. Quantum Electron. **38**, 495 (2006).
4. M. G. Thompson, A. R. Rae, M. Xia, R. V. Penty, and I. H. White, IEEE J. Sel. Top. Quantum Electron. **15**, 661 (2009).
5. C. Otto, K. Ludge, A. G. Vladimirov, M. Wolfrum, and E. Scholl, New J. Phys. **14**, 113033 (2012).
6. J. Rahimi, V. Ahmadi, and M. H. Yavari, Appl. Opt. **55**, 5102 (2016).
7. M. L. Davenport, S. Liu, and J. E. Bowers, Photonics Res. **6**, 468 (2018).
8. A. S. Bhushan, P. Kelkar, and B. Jalali, Electron. Lett. **36**, 1526 (2000).
9. B. K. Mathason and P. J. Delfyett, J. Lightwave Technol. **18**, 1111 (2000).
10. T. Yilmaz, C. M. DePriest, and P. J. Delfyett, Electron. Lett. **37**, 1338 (2001).
11. S. Srinivasan, A. Arrighi, J. R. Heck, J. Hutchinson, E. Norberg, G. Fish, and J. E. Bowers, IEEE J. Sel. Top. Quantum Electron. **20**, 8 (2014).
12. S. Keyvaninia, S. Uvin, M. Tassaert, X. Fu, S. Latkowski, J. Mariën, L. Thomassen, F. Lelarge, G. Duan, P. Verheyen, G. Lepage, J. V. Campenhout, E. Bente, and G. Roelkens, Opt. Express **23**, 3221 (2015).
13. M. C. Lo, R. Guzmán, and G. Carpintero, Opt. Lett. **43**, 507 (2018).
14. M. Shekarpour and M. H. Yavari, in *20th International Conference on Numerical Simulation of Optoelectronic Devices (NUSOD)* (2020), Vol. **75**.
15. A. Yariv and P. Yeh, *Photonics: Optical Electronics in Modern Communications*, 6th ed. (Oxford University, 2006).
16. D. A. Yanson, M. W. Street, S. D. McDougall, I. G. Thayne, J. H. Marsh, and E. A. Avrutin, IEEE J. Quantum Electron. **38**, 1 (2002).
17. A. G. Vladimirov and D. Turaev, Phys. Rev. A **72**, 033808 (2005).
18. D. J. Jones, L. M. Zhang, J. E. Carroll, and D. D. Marcenac, IEEE J. Quantum Electron. **31**, 1051 (1995).
19. L. A. Coldren, S. W. Corzine, and M. Mashanovitch, *Diode Lasers and Photonic Integrated Circuits*, 2nd ed. (Wiley, 2012).
20. J. Mulet and J. Mork, IEEE J. Quantum Electron. **42**, 249 (2006).